Colloidal stability over months of highly crystalline high-pressure high-temperature hydrogenated nanodiamonds in water

Lorris Saoudi, Hugues Girard, Eric Larquet, Michel Mermoux, Jocelyne Leroy, Jean-Charles Arnault

Version of Record: https://www.sciencedirect.com/science/article/pii/S0008622322009058
Manuscript_f1d801df2c20199043a8e771ebf1ba73

Colloid stability over months of highly crystalline high-pressure high-temperature hydrogenated nanodiamonds in water

Lorris Saoudi[1], Hugues Girard[1], Eric Larquet[2], Michel Mermoux[3], Jocelyne Leroy[1], Jean-Charles Arnault[1*]

[1] Université Paris-Saclay, CEA, CNRS, NIMBE, CEDEX, 91 191 Gif-Sur-Yvette, France

[2] Condensed Matter Physics Laboratory (PMC), UMR CNRS 7643, Ecole Polytechnique, IP-Paris, 91228 Palaiseau, France

[3] Univ. Grenoble Alpes, Univ. Savoie Mont Blanc, CNRS, Grenoble INP, LEPMI, 38000, Grenoble, France

* Corresponding author: jean-charles.arnault@cea.fr, +33169087102

Keywords : milled ND ; hydrogenation ; colloidal organization ; facets

Abstract

In this study, milled nanodiamonds synthesized from HPHT diamond (MND) were successfully hydrogenated and stabilized in colloidal suspension in water over months. The optimal hydrogenation conditions correspond to a minimization of carbon/oxygen bonds and sp^2/amorphous carbon at MND surface as shown by FTIR and XPS. Clean crystalline particles were observed by HR-TEM. The colloidal stability is discussed in terms of sp^2 carbon and role of facets. The signature of a surface conductivity was identified by FTIR. A particular arrangement in colloidal suspension of H-MND was observed by Cryo-EM for H-MND with the formation of chain like structures extending over micron range.

1. Introduction

Diamond nanoparticles or nanodiamonds (ND) are nowadays actively investigated for major fields of applications like drug delivery, photo(electro)catalysis, quantum devices, advanced lubricants and composites [1]. Among involved materials, nanodiamonds milled from bulk HPHT, CVD or natural diamond (MND) and detonation nanodiamonds (DND) behave very different assets [2-4]. Indeed, the crystalline quality and the size (tens of nm) of MND can explain their optical or electronic properties closer to performances of bulk diamond. In addition, milled and detonation nanodiamonds exhibit

significant differences in their shape (rounded or facetted), in the nature and the concentrations of impurities incorporated in the diamond lattice during synthesis. Such differences were recently highlighted comparing MND and DND of a few nm [5]. Consequently, each material is preferentially used for certain applications. For example, spin properties conferred by color centers hosted in MND are exploited for quantum applications [6] whereas the nanometric size of DND is a key asset for its clearance needed in drug delivery applications [7]. Surface properties of MND may also get closer to those of bulk diamond, especially their tuning with terminations by different heteroatoms (H, O, F, Cl,…) or functional groups [8]. In particular, the related band structures evolve with surface chemistry. In that sense, hydrogenation of MND surface has a particular interest to confer the negative electron affinity (NEA) [9] and the surface transfer doping properties well known for hydrogenated bulk diamond [10]. A photocatalytic effect, based on emission of solvated electrons, was shown for H-MND illuminated under UV leading to the CO_2 reduction into CO [11].

In most of application fields of ND, the control of colloids is of primary importance. There is a crucial need to reach a standardization for various industrial uses [12]. In studies related to bioapplications, additives are used to stabilize ND in physiological media like polymeric coatings [13], Bovine Serum Albumine (BSA) [14] or organic molecules like citric acid, oxalic acid, glutamic acid and propylamine [15]. Nevertheless, a fine control of the extreme surface chemistry can allow a stabilization of ND in water without any additive. Carboxylated DND in water exhibit a negative zeta potential within a wide pH range linked to the deprotonation of carboxyl acids into carboxylates [16]. On the other hand, surface graphitized [17] and hydrogenated [18] DND behave a positive zeta potential in water and stable colloids were reported. These positively charged DND were previously used to load and deliver siRNA conjugates to Ewing sarcoma tumor [19]. The origin of the positive zeta potential for H-DND is still a matter of debate: Petit et al. via a spectroscopic approach attributed it to a specific organization of water molecules surrounding H-DND leading to a charge transfer at the interface [20]. The specific interaction of H-DND with water molecules was confirmed by Stehlik et al. with the possible formation of water nanodroplets into DND aggregates [21]. A second origin was proposed based on with the protonation of graphitic reconstructions present at H-DND surface [22].

In the case of MND, if the colloidal properties for carboxylated MND in water are well described [5], only scarce studies were up to now reported for hydrogenated MND. A previous investigation concludes that graphitic reconstructions are a prerequisite to confer colloidal stability to H-MND in water [22]. Nevertheless, in this study, no time monitoring of colloids of H-MND was provided.

The surface of detonation ND can be efficiently hydrogenated either by an exposure to microwave plasma [16] or by thermal treatment at 500°C [23–25]. H-DND are then stabilized in water exhibiting a high positive zeta potential (> +60 mV) and a very good stability in time (several months). Conversely, MND hydrogenated at the same temperature cannot be stabilized in water even increasing hydrogen pressure up to the atmospheric pressure and using longer duration. The present study aims to reach a colloidal stability for H-MND in water over months. For this purpose, it finely investigates the colloidal assets of H-MND suspended in water versus the hydrogenation conditions (temperature and hydrogen pressure). To better understand origins that confer stability in water, the surface chemistry of the different H-MND samples was extensively characterized combining FTIR, XPS, UV Raman, XRD and HR-TEM experiments. Cryo-EM and DLS/zeta measurements gave access to the spatial repartition of H-MND in water, the hydrodynamic diameter and zeta potential measurements, respectively. Contrary to oxidized MND, the formation of chains extending at long range involving facets of H-MND was evidenced. XPS, HR-TEM and UV-Raman confirmed an almost complete removal of oxidized functional groups after hydrogenation at 750°C under atmospheric pressure. A very low amount of sp^2 carbon was measured by UV Raman and XPS on H-MND. HR-TEM observations revealed a clean hydrogenated diamond surface. Finally, from valence band analysis by XPS and IR spectroscopy, we also evidenced a modification of the energetic diagram of our H-MND and the formation of a conductive layer at their surface as for bulk material. Such stable aqueous colloids open the way to use H-MND for quantum and photo(electro)catalysis applications.

2. Material and methods

Nanodiamonds and preparation of aqueous colloids

Milled nanodiamonds SYP 0-0.05 (purity > 99.9 %) were purchased from Van Moppes (Switzerland). Sonication was performed on 100 mg of powder (as received, oxidized or hydrogen-annealed) disposed in a 15 mL plastic tube filled with 2.5 mL of ultrapure water (18.2 MΩ.cm) using a Cup Horn Bioblock Scientific 750 W system, equipped with a cooling system which maintains a constant temperature of 10°C all along the ultrasonic treatment. Sonication was realized for 30 min with a 1 s on/off period and an amplitude of 60%. In these conditions, the ultrasonic power delivered to water has been estimated to 30W via a calorimetric method. The slurry obtained after sonication was then centrifuged for 40 min at 2400g. The supernatant was immediately collected at the end of the centrifugation to avoid spontaneous re-dispersion of the sediment in the upper phase. Sediments and supernatants were then stocked in plastic

vials at room temperature. Concentration of the colloids were measured by weighting the residue of a known volume of supernatant dried overnight at room temperature.

Thermal treatments

Annealing treatments were realized in a tubular furnace purchased for Carbolite Gero Company (Sheffield, UK)). For oxidation (Ox-MND), 600 mg of as-received nanodiamonds were treated at the same time, divided into two alumina crucibles. The annealing was performed under air at atmospheric pressure using a ramp of 10°C/min up to 480°C for 5h. For hydrogenation (H-MND), 150 mg of Ox-MND were placed in a quartz tube flowed with dihydrogen gas (Air Products 5.0) at 50 sccm. A first desorption step at 200°C for 30 min was systematically performed before reaching at 30°C/min the defined annealing temperature (600°C, 650°C, 700°C or 750°C) maintained for 5h. Hydrogenations were realized either at atmospheric pressure of H_2 or under low pressures (10 and 100 mbar) using a dedicated pumping system with pressure regulation.

Infrared spectroscopy

Infrared spectra were recorded with a Bruker Alpha II spectrometer equipped with a Platinum ATR system (diamond crystal). For a typical measure, 2 µL of MND of the colloid or the sediment (before drying of the water content) were deposited on the ATR crystal and allow to dry under a flow of dry nitrogen (≈ 1L/min) for few minutes. Spectra acquisition was realized while keeping the nitrogen flow with a resolution of 4 cm^{-1}. Spectra given in the present study are the average of 128 scans for the sample and 64 scans for the background (clean ATR crystal under N_2 flow), without any correction of the baseline.

X-ray Photoemission Spectroscopy

A measure of 10 µL of DND in water was deposited on a silicon substrate covered by a gold coating made by evaporation to limit the charge phenomenon during analysis. The substrates were dried and then analyzed. XPS measurements were performed on a Kratos Analytical Axis Ultra DLD spectrometer equipped with a monochromated Al Kα (1486.6 eV) X-ray source and a charge compensation system (Manchester, UK). The take-off angle was set at 90° relative to the sample surface. Spectra were acquired at a pass energy of 160 eV for the survey, 40 eV for core levels (O 1s, C 1s). C 1s spectra shown in this study were acquired at 10 eV to reach a higher energy resolution. Binding energies were referenced to the $Au4f_{7/2}$ peak located at 84 eV. Valence band spectra were recorded at a pass energy of 20 eV. After the background subtraction by a Shirley correction, a curve fitting procedure was carried out to extract the components of the C1s core level using Voigt functions with a Lorentzian to Gaussian ratio of 30%.

X-Ray Diffraction

The X-Ray diffractograms were recorded using a Bruker-2D-Phaser diffractometer, in the 2θ range 10° - 100° with a Cu X-ray source (Kα = 1.5406 Å), step size of 0.065° and a counting time per step of 4 s. Analyses were realized on ≈10 mg of powder were deposited onto a silicon wafer.

High resolution Transmission Electron Microscopy

Transmission Electron Microscopy (TEM) have been performed on a ThermoFischer Scientific™ G3 Titan Themis 300 transmission electron microscope (C-Twin objective lens: Cs = 2.7 mm, Cc = 2.7 mm, Focal length = 3.5 mm) operating at 300 kV accelerating voltage. Prior to the observation, the DND were deposited on a 200 mesh holey carbon film. High Resolution observations (HR-TEM) have been performed at 520,000x magnification for different defocus values (defocus range: −0.3 to −0.4 µm) using low dose mode on a ThermoFischer Scientific™ Falcon 3EC 4Kx4K Direct Detection Electron (DDE) camera. To best preserve samples from electron beam irradiation during image acquisition, a total electron dose of 25 $e^{-}/Å^{2}$ was used for a limited exposure time of 1 sec.

Cryo-Electron Microscopy

4 µl of colloidal suspensions were deposited on a 300 mesh lacey carbon-coated grid. After blotting with filter paper, the grid was frozen by rapid plunging in liquid ethane and was mounted and inserted in the microscope using a nitrogen-cooled side entry Gatan Elsa™ (698) Cryo-holder at a temperature of −181 °C. Observations were carried out in a ThermoFischer Scientific G3 Titan Themis 300 transmission electron microscope equipped with a Cryo-box anticontamination system and a C-Twin objective lens (Cs = 2.7 mm, Cc = 2.7 mm, Focal length = 3.5 mm), using an accelerating voltage of 300 kV, with the following illumination conditions: spot size of 5, a 150 µm condenser aperture, and no objective aperture. Images were recorded (defocus range: −0.3 to −0.4 µm), using the low electron dose system (10 $e^{-}/Å^{2}$ per sec), with a magnification of 5,400x and 58,000x on a ThermoFischer Scientific™ Falcon 3EC Direct Detection Electron 4Kx4K camera in linear mode.

Raman Spectroscopy

Samples were prepared by drop casting and drying of MND colloids on silicon substrates. A Ib diamond single crystal was used for calibration. Micro-Raman measurements were performed using a Renishaw InVia spectrometer in the near-UV (325 nm) spectral range. It is equipped with an air-cooled CCD detector, different specific gratings (1200 and 2400 grooves/mm), and dielectric rejection filters. Using the 325 nm excitation, the low frequency cut-off was at about 250 cm^{-1}, and the full width at half maximum of the reference diamond single crystal was close to 9 cm^{-1}. In the UV range, this spectrometer

was at first used for a fast, wide frequency range overview of the samples. For this particular wavelength, the spectral resolution was too low to enable a detailed analysis of the Raman diamond line profile. A UV-dedicated 40× objective (NA = 0.5) was used to focus the laser at the sample surface and collect the scattered light. A special care was taken to prevent unwanted temperature effect that may induce phonon peak downshifts, or even sample modification upon illumination. When working on nanoparticles, sample heating is a well-known issue, that strongly depends on the optical properties of the particles, thus on the excitation wavelength. The incident laser power was minimized below ≈50 $\mu W/\mu m^2$. A line excitation instead of a point excitation was used to reduce the sample irradiance while keeping a rather high signal to noise ratio. Using such conditions, "reasonable" acquisition time, between 60 s and 2400 s depending on the desired signal quality could be achieved.

Dynamic light scattering (DLS) and zeta potential measurements

Hydrodynamic diameters and zeta potentials were measured by dynamic light scattering and laser Doppler electrophoresis using a Horiba Nanopartica SZ100 system. Acquisitions were realized at 25°C with a 173°C backscattered angle on diluted suspensions (1 or 0.5 mg/mL) in ultrapure water (18.2 MΩ.cm) using automatic mode. Size distributions and Zeta measurements result from the average of 10 independent measurements. For measurements over two months, aperture values and filtering mode were set manually to ensure comparable measurements.

3. Results

3.1 Colloidal suspensions

Annealing under hydrogen atmosphere at temperatures ranging from 600°C to 750°C and pressures ranging from 10 mbar up to atmospheric pressure were applied to oxidized MND. Immediately after annealing, treated MND were systematically (i) sonicated for 30 min in ultra-pure water and (ii) centrifuged for 40 min. Depending on the sample, we were able to collect particles either in the supernatant (i.e. a colloidal suspension) and in the sediment or only in the sediment (no colloidal suspension) (see Table 1). Using this approach, we obtained colloidal suspensions of H-MND for annealing at temperature above 700°C whatever the pressure, with concentration ranging from 2.8 to 4.3 mg/mL (i.e. 0.28 to 0.43 wt %). For the 600°C and 650°C annealed MND, the supernatant was clear of particles, all of them being in the sediment. Following characterizations were then performed either on sediment or on supernatant, and on both when possible and relevant.

	600°C Patm	650°C Patm	700°C Patm	750°C Patm	750°C 100 mbar	750°C 10 mbar
Particles in the supernatant	No	No	Yes	Yes	Yes	Yes
Max concentration	-	-	3.7 mg/mL	4.3 mg/mL	3.4 mg/mL	2.8 mg/mL

Table 1 : Colloidal stability and concentration measurements for MND hydrogenated at 600°C, 650°C, 700°C and 750°C at atmospheric pressure (Patm), 100 mbar and 10 mbar. Uncertainties are estimated to ± 10 % for concentration values.

3.2 FTIR measurements

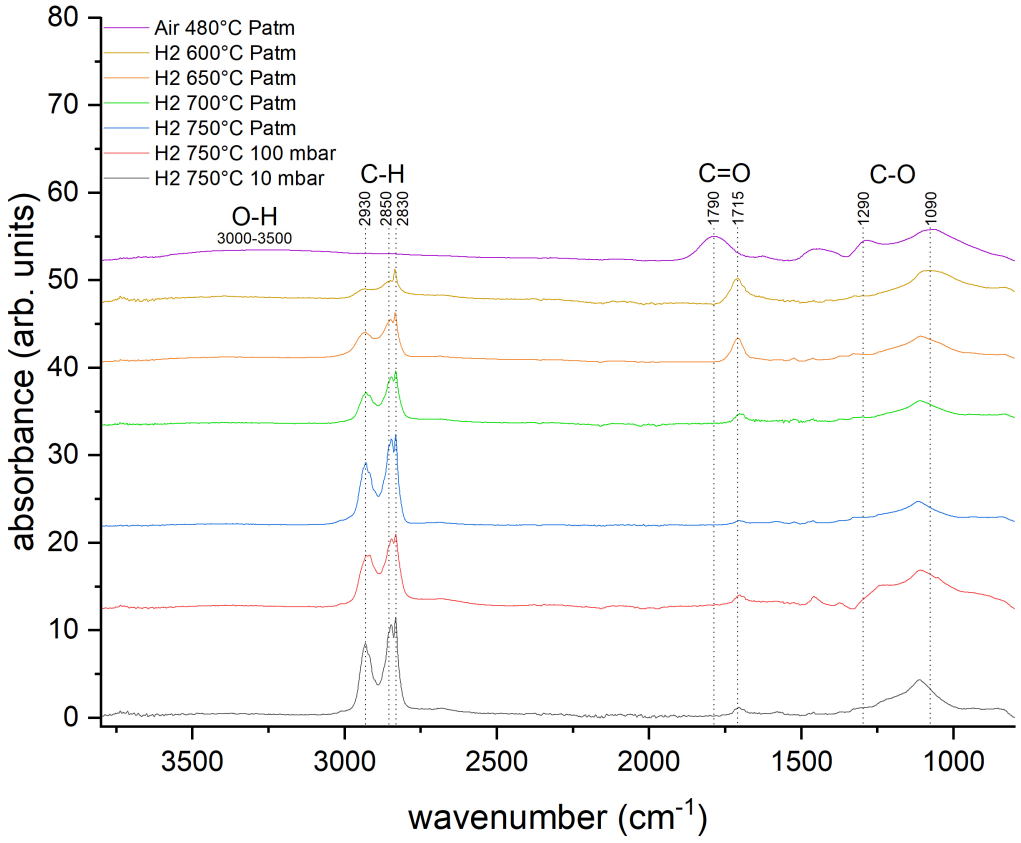

Figure 1 : FTIR spectra of sediments of Ox-MND and MND hydrogenated at 600°C, 650°C, 700°C and 750°C at atmospheric pressure (Patm), 100 mbar and 10 mbar.

To ensure a better-defined ND surface before hydrogenation, a cleaning of MND by oxidation under air annealing [26] was applied at a temperature of 480°C, adjusted from TGA experiment to limit the etching of the diamond core (SI, Figure S1). After this oxidation step, FTIR spectra of the particles present in the supernatant and in the sediment (Figure 1 & Figure 2) show typical features of oxidized ND, with (i) strong C=O stretching modes (centered at 1790 cm^{-1}) linked to ketones, carboxylic acids and anhydrides and (ii) O-H stretching and bending modes (3000-3500 cm^{-1} and 1630 cm^{-1} respectively). Note that on our spectrometer the deposited layer of MND on the ATR crystal is flushed with a dry nitrogen flow all along the analysis, thus we can expect a very limited contribution of water-related O-H vibrations. Additional features are clearly visible in the fingerprint area, with two peaks located at 1290 and 1090 cm^{-1}, attributed to C-O stretching modes of anhydrides and etheric groups respectively [27]. A last peak centered at 1450 cm^{-1} is also noticeable on the spectrum, not yet clearly attributed. Here, spectra of the supernatant and the sediment are strictly similar, which let us conclude that surface chemistry is not at the origin of their sedimentation, but rather the size of the aggregates.
On this oxidized sample, annealing under atmospheric pressure (Patm) of H_2 were then performed with rising temperature from 600°C to 750°C by 50°C increment. For the highest temperature, two more treatments under H_2 with a pressure reduced down to 100 mbar and 10 mbar were also realized. Note that for sake of clarity, all spectra were normalized at the 1300-1350 cm^{-1} area.

Let focus first on the analysis of the sediment, which allows us to compare all the treated samples. From 600°C, a shift of the C=O stretching mode is observed down to 1715 cm^{-1} as well as a complete vanishing of the 1290 cm^{-1} C-O peak and 3000-3500 cm^{-1} O-H band. This evolution signs for the reduction of anhydrides/carboxylic acids to ketones. Then, with the rise of the hydrogenation temperature, the intensity of the C=O stretching mode drastically decreases, followed by the simultaneous partial reduction of the C-O bands around 1100-1300 cm^{-1}. After annealing at 750°C under atmospheric pressure, samples do not exhibit any more carbonyl groups, only C-O stretching modes presumably associated to etheric/epoxy functions remain at the MND surface. However, when the pressure is reduced down to 100 mbar and 10 mbar at the same temperature, it can be noticed that some carbonyl functions remains.

In parallel, C-H stretching modes between 2800 and 3000 cm^{-1} associated to CHx groups on aliphatic carbons [24] are clearly present on H-MND whatever the hydrogenation temperature/pressure. Nevertheless, their related fine structure evolves versus the temperature, with the progressive increase of the 2930 cm^{-1} and 2850 cm^{-1} features while the peak at 2830 cm^{-1} always stays the more intense. The more precise assignation of these peaks will be further discussed. Here, we do not detect any influence of the pressure on the C-H stretching shape.

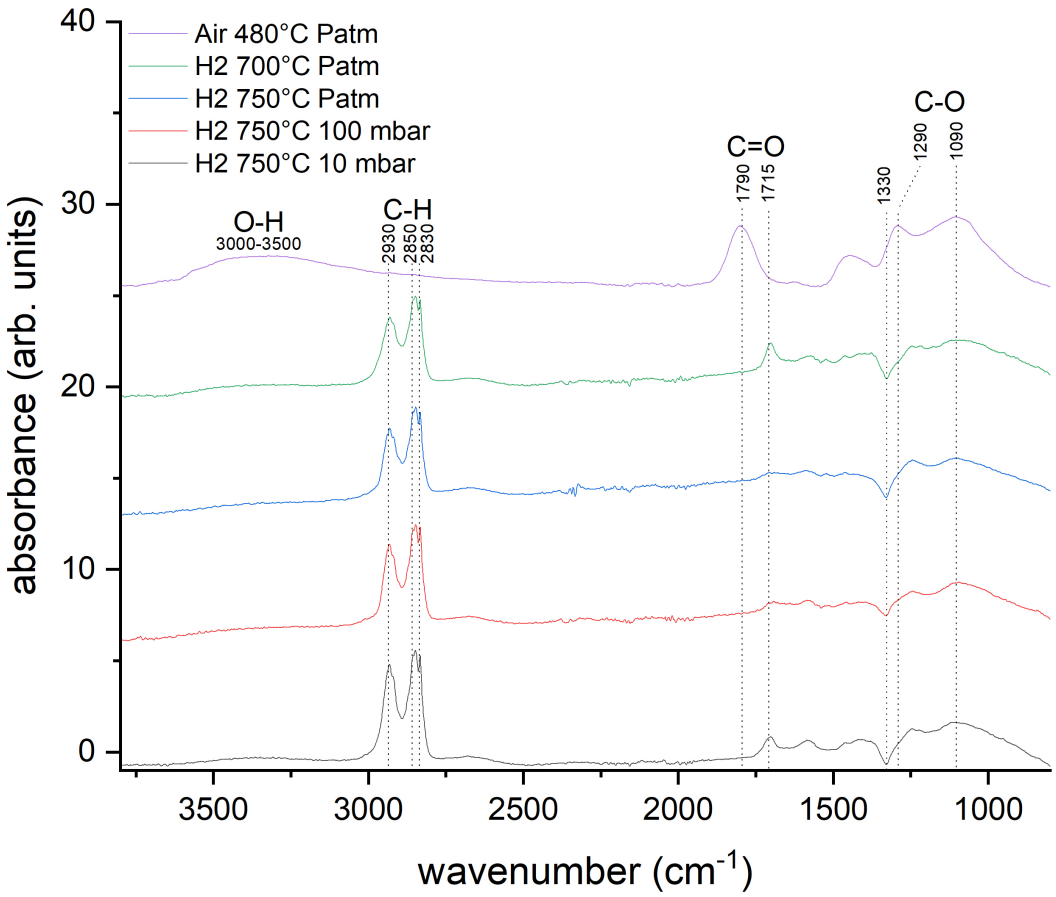

Figure 2: FTIR spectra of colloids of Ox-MND and hydrogenated MND at 700°C and 750°C at Patm, 100 mbar and 10mbar.

Now, let discuss about the FTIR spectra recorded from the supernatants of samples treated at 700°C and 750°C (Patm, 100 and 10 mbar) and available on Figure 2. Concerning the C=O and C-O stretching modes, the particles in colloidal suspension exhibit the same evolution than unstable particles, with the almost complete removal of oxidized terminations from their surface. Here as well, a small effect of the hydrogen pressure during the annealing at 750°C is evidenced with the remaining of a weak C=O signature. More significant, looking at the C-H stretching bands associated to CHx functions, it can be noticed that the ratio between the 2850 and 2930 cm^{-1} peaks and the one at 2830 cm^{-1} is modified if we compare with the sediment, the latter being now less intense for all recorded spectra. A second important difference between the colloids and the sediments concerns the dip in the spectrum visible at 1330 cm^{-1}, clearly visible on all spectra made on supernatants. The origin of this particular IR feature will be later discussed.

3.2 XPS analysis

The XPS wide scan of as received and oxidized MND only exhibits carbon and oxygen core levels (SI, Figure S2). Contrary to DND, the nitrogen is not detected meaning its atomic concentration is under the XPS detection limit (< 0.5 at %) [28]. For Ox-MND, the oxygen atomic concentration is of 9.4 at % (Table 2). The decrease of the carbon-oxygen bonds from the MND surface with the hydrogenation temperature as seen by IR spectroscopy is then confirmed by the XPS analysis. From 9.4 at %, the oxygen content is reduced down to 1 at % at 750°C at Patm. Note that the use of atmospheric pressure allows a minimization of residual oxygen while the oxygen concentration remains at 2.5 at % for a pressure of 10 mbar.

	Ox-MND Air 480°C Patm	HMN-D H_2 600°C Patm	H-MND H_2 650°C Patm	H-MND H_2 750°C Patm	H-MND H2 750°C 100 mbar	H-MND H_2 750°C 10 mbar
	Atomic concentrations (at %)					
Carbon	90.6	96.8	98.0	99.0	97.5	97.5
Oxygen	9.4	3.2	2.0	1.0	2.5	2.5
	% of total carbon in C1s core level					
C sp^2 (- 1 eV)	4	1.4	1.2	1	1.5	1
C sp^3	76	82.8	87.9	80	83	81
C-H_x. C-$C_{defects}$ (+ 0.8-0.9 eV)	11	9.8	9	16	10.5	11
C-OH (+ 1.2 eV)	2	1.7	0.8	0.5	1.5	5
C-O-C (+ 1.9 eV)	4	2.6	1.1	2	2.5	1.5
C=O & COOC (+3,0-3,9 eV)	3,5	1.7	0	0.5	1	0.5

Table 2: Elemental composition and percentage of total carbon in C1s core level of the different carbon and carbon-oxygen bonds for oxidized MND and MND hydrogenated at different temperatures and pressures. Uncertainties are estimated to ± 2.5 % and ± 5 % for atomic concentrations and amounts of components extracted from fitting, respectively. Measurements were realized on supernatants except for the H-MND 600°C and H-MND 650°C done on the sediments.

C1s core level deconvolution provides us more insights on the surface chemistry of treated MND. By way of example, two fits of the C1s core level are provided on Figure 3 for Ox-MND and H-MND (750°C at Patm), while values of all the deconvolutions are gathered in Table 2. Considering the sp^3-carbon component is a reference, the asymmetric sp^2-carbon contribution is located at -1 eV [17], while the one related to CH_x and C-C defects is at + 0.8-0.9 eV [29]. Several components are corresponding to carbon/oxygen bonds: single bonds at +1.2 eV (C-OH) and +1.9 eV (C-O-C), double bonds at +3 eV (C=O) and +3.9 eV (COOC) [30].

For Ox-MND, apart the presence of C-O and C=O related components in agreement with the IR spectroscopy, the fit of the C1s core level revealed a sp^2-carbon contribution of 4 % from total C1s intensity. This value has to be compared to the initial contribution of 8.5 % of sp^2 carbon for the as received MND (SI, Figure S3). Our pre-oxidation step has thus significantly (but not completely) reduced the non-diamond carbon present at MND surface.

For hydrogen-treated samples, the evolution of the carbon C1s core level spectra confirm the drop of oxygen content and the evolution of the IR spectra, with the decrease of C-OH/C-O-C and C=O/COOC components with the annealing temperature (SI, Figure S3). XPS analysis also exhibits the almost complete etching of the remaining graphitic carbon thanks to the hydrogen atmosphere (from 4 % to 1 % of the overall carbon). Finally, we can also notice a significant increase from 11 to 16% of the component related to $C-H_x$ and C-C defects for the harsher hydrogenation conditions (750°C and Patm).

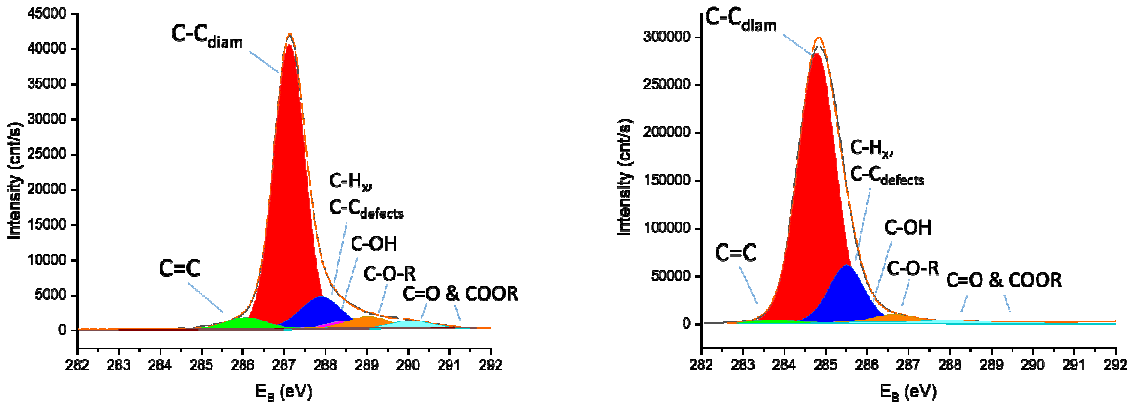

Figure 3: XPS C1s spectra of Ox-MND (left) and Ox-MND hydrogenated at 750°C and Patm (right)

The binding energy position of the sp^3-carbon component underwent a downshift of - 2.3 eV after hydrogenation. The origin of this shift will be later discussed.

3.3 HR-TEM analysis

HR-TEM observations of Ox-MND and H-MND (750°C Patm), both from colloids, are presented in Figure 4. For each sample, a large number of particles where thoroughly investigated, only four of them are reported here but chosen to represent at the best the diversity of observed morphologies. Note that a clear polydispersity in diameter has also been noticed, this aspect will be discussed more in details when dealing with Cryo-Electron Microscopy (Cryo-EM) (paragraph 3.5.2).

As expected, these milled nanodiamonds exhibit sharp edges and facets. For Ox-MND, we noticed a non-negligible amount of particles behaving amorphous and/or graphitic carbon at the periphery of their diamond core (Figure 4, top-left picture), while some others exhibited cleaner surface (Figure 4, top-right picture). On the contrary, on almost all H-MND, (111) diamond planes were seen to reach the extreme surface of the nanocrystal, without noticeable presence of non-diamond carbon. These observations are in agreement with the XPS analysis, which already evidenced an almost complete reduction of the sp^2 content after hydrogenation, from 4 to 1 at % (Table 2).

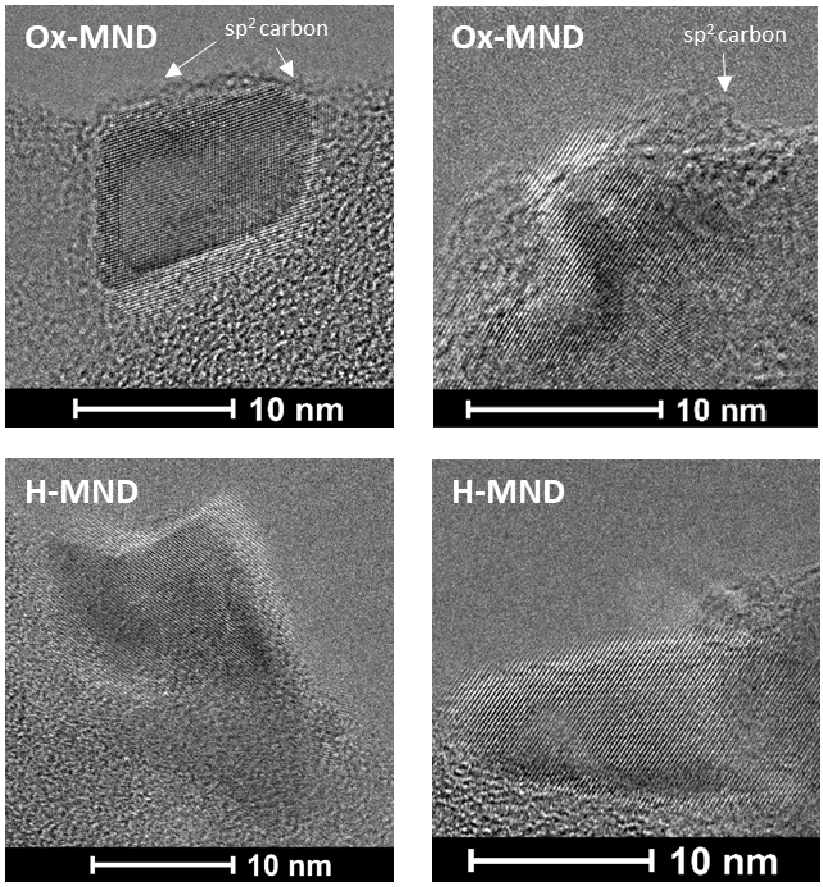

Figure 4 : HR-TEM pictures of Ox-MND (top) and H-MND hydrogenated at atmospheric pressure and 750°C (bottom)

3.4 Raman spectroscopy

Raman observations of these two samples were performed as an attempt to probe the sp^2 and sp^3 carbon contributions. On diamond nanoparticles, using 325 nm excitation wavelength allows to reduce the photoluminescence background compared to more conventional excitation at 532 nm or 785 nm. Moreover, at such a wavelength, the sp^2 carbon contribution is not strongly exalted compared to the sp^3 one [31, 32]. Spectra are compared in Figure 5. For both samples, the diamond Raman zone-center is clearly observed at 1332 cm^{-1}. The maximum observed around 1600 cm^{-1}, common to both samples, suggests the presence of some disordered graphite. If we consider the ratio of this G band to the first order diamond peak, we can notice that it is higher for the hydrogenated sample. The comparison with previous XPS and HRTEM results will be made in the part 4. Note that at 325 nm, the D band has almost vanished [33]. It also appears that the signal is much wider and more asymmetric towards the high frequencies for the oxidized sample. As mentioned in the literature, this signal falls within the expected frequency range for carbonyl or carboxylic functions, in agreement with our XPS and FTIR analysis [34].

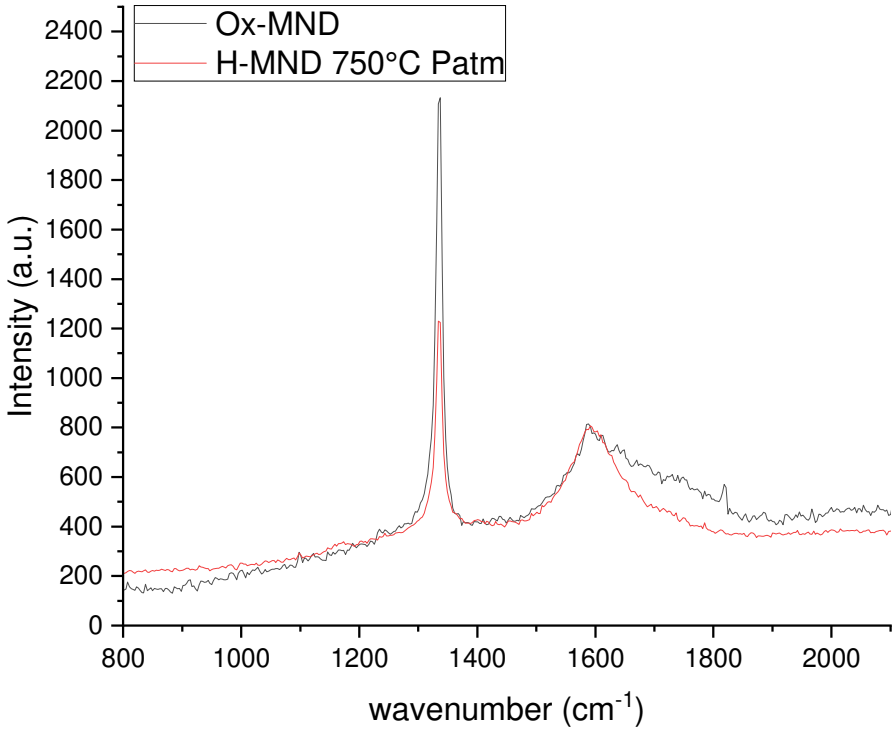

Figure 5: Raman spectra of Ox-MND and H-MND hydrogenated at 750°C and Patm recorded at a wavelength of 325 nm. Signals have been normalized to the intensity measured at 1600 cm^{-1}, for comparison purposes.

3.5 Time monitoring of colloidal properties and spatial arrangement of H-MND in water

3.5.1 Monitoring of the colloidal properties (from one day to two months)

Hydrodynamic diameter distributions and Zeta Potential measurements were performed on the colloids, one day after being put in suspension but also during two months later to check their long-term stability. During this period, no agitation or mixing was applied to suspensions. Results are gathered on Figure 6, Figure 7 and Figure 8.

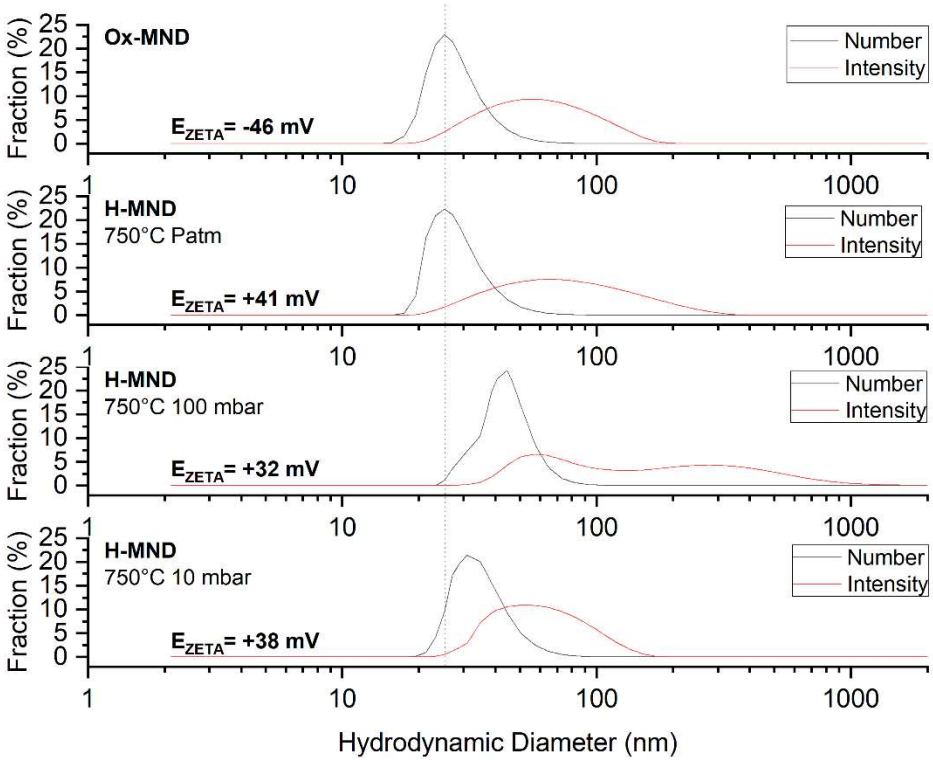

Figure 6: Distributions of hydrodynamic diameters measured at one day on the oxidized MND and after hydrogenation at 750°C for different pressures of H_2

On Figure 6, distributions of hydrodynamic diameters are first represented in fraction of the scattered light intensity. In this representation, the polydispersity of our particles is not taken into account and the proportion of the largest objects is exalted (light scattering is proportional to the particle radius at a power of 6 [35]). Here, we can notice that our suspensions do not contained particles or aggregates with diameters exceeding 200-300 nm whatever the surface chemistry, except for the 100 mbar. Now, looking at the corrected distribution by number of particles, it appears that most of the objects in suspension exhibit diameters ranging from 5 to 40 nm, with a maximum around 25-30 nm. Up to now, hydrogenated

MND exhibit almost similar colloidal distribution in water than oxidized MND, at least as it is shown by DLS.

Concerning the Zeta Potentials of our particles, as for detonation nanodiamonds [16] we observe a switch from a negative value for oxidized particles (explained by the presence of carboxylates on their surface) to positive values when hydrogenated, whatever the pressure during the annealing.

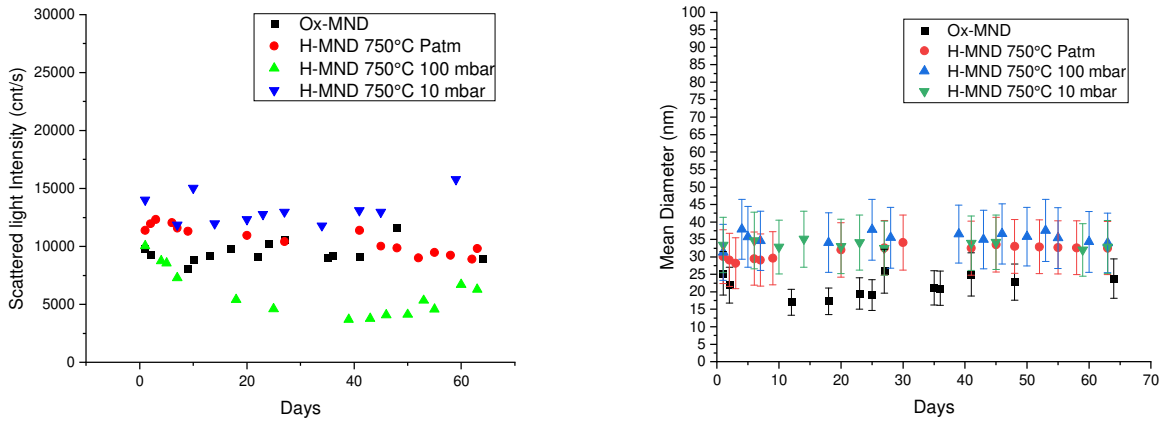

Figure 7: Scattered light intensities (left) and mean hydrodynamic diameters (right) measured by DLS over 2 months for Ox-MND and H-MND at 750°C and different hydrogen pressures

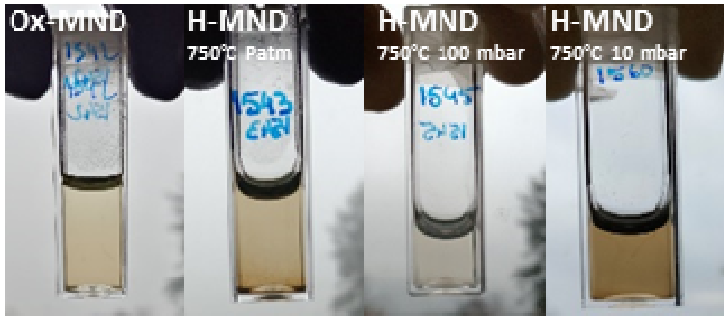

Figure 8 : Ox-MND and H-MND suspensions in water after 2 months, diluted at 1 mg/mL except the 750°C 100 mbar diluted at 0.5 mg/mL

The good colloidal stability of the different H-MND in water was further confirmed by a regular monitoring of the backscattered light intensity for the three suspensions and compared to the Ox-MND suspension (Figure 7). In addition, pictures of suspensions after 2 months are given in Figure 8. The backscattered light intensity is sensitive to the amount of particles in suspension and to their size. Therefore, a variation will translate either an aggregation phenomenon and/or a sedimentation. Here, the intensities were found almost constant during two months for Ox-MND and H-MND 10 mbar. For H-MND Patm, a slight decrease of the scattered intensity occurred (-15% after 2 months), probably due to a

limited sedimentation, which may be seen on figure 8 at the bottom of the cell. For the MND hydrogenated at 100 mbar, the backscattered light intensity exhibited a different trend without clear explanation at this time (see Figure 7). In parallel, DLS measurements revealed that the mean diameter of the objects in the suspension remained constant around 30 nm over the two months (Figure 7).

3.5.2 Spatial arrangement of H-MND in water

To better characterize the aqueous suspensions of H-MND (750°C/Patm), it is required to assess the spatial repartition of particles. For this purpose, H-MND in water were investigated by cryo-EM and compared with Ox-MND. To reach comparable density of particles on cryo-EM images, suspensions concentrated at 0.6 mg/mL and 12 mg/mL were needed for H-MND and Ox-MND, respectively. Typical images are presented on Figure 9.

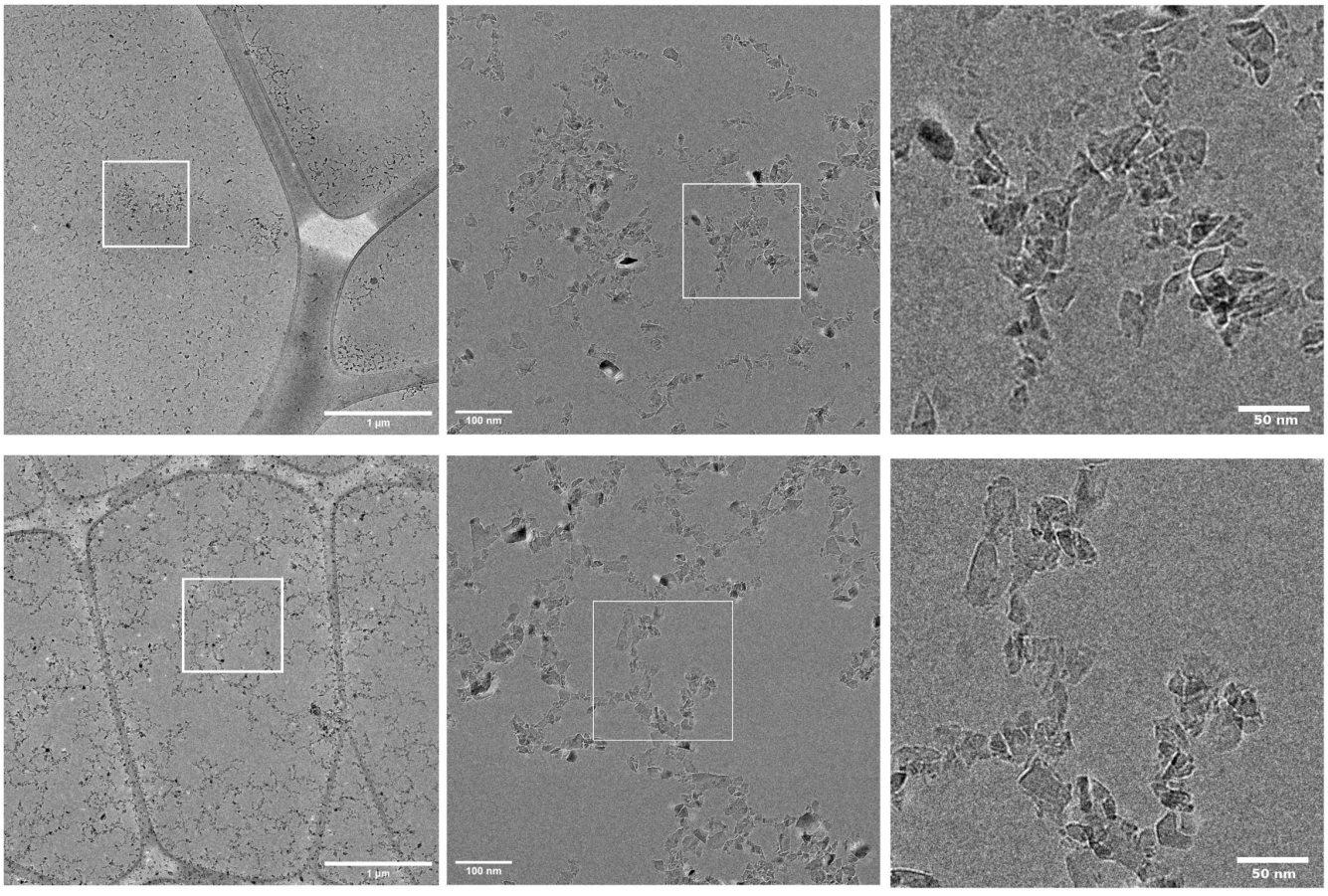

Figure 9 : Cryo-EM observations of Ox-MND (top) and H-MND at 750°C and atmospheric pressure (bottom) suspended in water

On the left, observations on large areas allow to estimate the homogeneity of MND repartition in ice. H-MND exhibit a homogeneous spatial repartition over micron sizes while Ox-MND reveal highly

heterogeneous. The density of Ox-MND seems to be very sensitive to the ice thickness with a much larger proportion of particles located in thicker ice. This affinity of Ox-MND for thick ice layers explains the necessity to increase the concentration of the suspension, in order to keep sufficient density of particles in thin ice areas where cryo-EM can be performed.

Looking to the spatial repartition at higher resolution (Figure 9, middle and right side), chain-like structures extending on large areas are evidenced for H-MND hydrogenated at 750°C and Patm. Such chains can involve several tens of particles of different sizes. The length of those chains can reach several hundreds of nm and facets of H-MND seem to be involved in this specific arrangement. Homogeneous chain patterns are obtained at large scale for H-MND, contrary to Ox-MND (Figure 9, left side). Note that a similar chain like structure was also evidenced for MND hydrogenated under 100 mbar at 750°C (SI, Figure S4). The origin of this particular behavior will be later discussed. For pre-oxidized MND, the spatial repartition looks more heterogeneous with isolated particles, aggregates involving tens of particles and small chains within the ice layer.

4. Discussion

4.1 Effect of hydrogenation conditions on surface chemistry of MND

The expected effects of hydrogenation treatment on MND surface chemistry are the reduction of carbon/oxygen functional groups, the etching of non-diamond carbon (graphitic and/or amorphous) and the formation of C-H bonds on diamond facets of MND.

FTIR and XPS investigations performed on pre-oxidized MND hydrogenated from 600°C to 750°C well evidence a progressive reduction of C=O and C-O functional groups at MND surface (Figure 1 and Table 2). FTIR spectra exhibit a downshift of the C=O stretching mode that corresponds to the reduction of anhydrides/carboxylic acids into ketones. It is worth noting that the amount of remaining carbonyls seems to be dependent on the hydrogenation pressure. The total oxygen atomic concentration measured by XPS drops from 9.4 at % for pre-oxidized MND to 3.2 at % and 1 at %, for H-MND at 600°C and 750°C, respectively. When lower pressures are used for hydrogenation, the remaining oxygen concentration is significantly higher at 2.5 at % showing a less efficient reduction. The evolution of C=O & COOR component in C1s core level is in fair agreement with FTIR results. For C-O components (C-OH and C-O-C), despite a decreasing tendency with temperature, the evolution looks less obvious.

Very low amount of sp^2 carbon is measured by XPS whatever the hydrogenation conditions, with a moderate reduction from 4 % of the total C1s area for oxidized MND to 1-1.5 % for H-MND. However,

at the same time, UV Raman results express a measurable increase of disordered and graphitic carbons (G band) for H-MND (750°C / Patm) compared to oxidized ones (Figure 5). The quantification in Raman spectroscopy remains complicated, considering that the cross section ratio of the sp^2/sp^3 carbon is strongly dependent on the excitation wavelength. Therefore, the apparent opposite evolution of XPS and Raman signals finally concerns weak amounts of sp^2 carbon. This low amount of sp^2 carbon at the surface of H-MND was also confirmed by HR-TEM images (Figure 4) that reveal clean facets and (111) diamond planes reaching the surface of particles (even if HR-TEM is a very local technique and concerns only a limited number of particles).

If the formation of C-H bonds at MND surface starts from 600°C, different structures of C-H stretching modes are observed in FTIR (Figure 1 and Figure 2) when the hydrogenation temperature increases. We observed an evolution between the relative intensities of the three main peaks of the structure, located at 2930, 2850 and 2830 cm^{-1}. Concerning the precise assignment of these peaks, 2930 and 2850 cm^{-1} features should correspond to the symmetric and asymmetric stretching vibration of CH_2 groups if we consider the literature on infrared spectra of organic compounds [36] and the pioneering work of Jiang et al. [37] on hydrogenated detonation nanodiamonds. Nevertheless, our nanodiamonds were synthesized by milling of High Pressure High Temperature diamond material, and several studies dedicated to this type of particles were published in the early 2000s [38, 39, 40]. They underline the specificity of the C-H stretching vibration structures of diamond nanoparticles larger than detonation nanodiamonds (≈5 nm), considering the appearance of well-defined crystal facets when the size of the particle increase. From this point of view, the peak located at 2930 cm^{-1} corresponds to the C-H terminations on (100) surface, the peak at 2850 cm^{-1} to the C-H terminations on (110) surface and the one at at 2830 cm^{-1} to the C-H terminations on (111) surface. If we now focus on the evolution of these peaks according to the annealing temperature, we noticed that at 600°C and 650°C, the main feature is detected at 2830 cm^{-1}, i.e. hydrogen terminations on (111) facets. At higher temperatures, two additional features appear at 2930 cm^{-1} and 2850 cm^{-1} corresponding to hydrogen termination on (100) and (110) facets, respectively. At 750°C, those features are clearly resolved. Note that the C-H mode relative to the (111) facet at 2830 cm^{-1} remain the main one for sediments contrary to supernatants. This aspect will be considered when discussing the colloidal stability of H-MND. Another important aspect concerns the amount of C-H bonds formed at MND surface versus temperature and pressure. No quantitative measurements have been reached at this stage but the significant increase of the C-Hx, C-C defects component in C1s core level in XPS for 750°C and Patm may be a first indication of a higher density of C-H bonds (Table 2).

For the sample hydrogenated at 750°C and Patm, an energy shift of the sp^3 component (- 2.3 eV) was observed in the C1s XPS core level (Figure 3). Complementary measurements performed at the valence

band confirm this downshift for MND hydrogenated at 750°C whatever the hydrogenation pressure (Figure 10). The upper part of the valence band is located at 2.3 eV lower binding energy compared to pre-oxidized MND . If spectra are artificially shifted for an easier comparison with preoxidized MND, the progressive decrease of oxygen with the hydrogenation pressure is well illustrated on the O2s photoemission peak at 28 eV. For each spectrum, the components located at 13 eV and 20 eV are assigned to a diamond fingerprint and to the C2s photoemission peak, respectively [41]. The decrease of sp^2 carbon measured at C1s core level is in agreement with the disappearance of the feature located at 11 eV for oxidized MND, previously assigned to non-diamond carbon [42]. This downshift of the valence band and of the sp^3 component at C1s core level expresses a modification of the band structure for hydrogenated MND. The same trend was previously observed for bulk diamond [43].

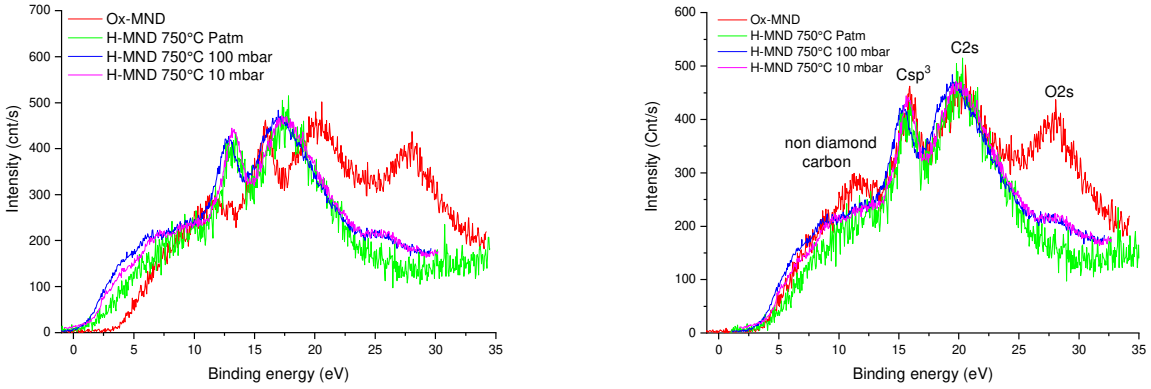

Figure 10: Valence band spectra of Ox-MND and MND hydrogenated at 750°C for different pressures (left), for an easier comparison, spectra were artificially shifted (right)

In summary, the hydrogenation temperature is the main parameter that controls the MND surface chemistry. At 750°C, an efficient reduction of carbon/oxygen functional groups and of non-diamond carbon is obtained. The sole advantage of atmospheric pressure at this temperature is to allow a stronger reduction of oxygen functional groups at H-MND surface. Whatever the hydrogenation pressure, a downshift of the band structure is observed for H-MND compared to Ox-MND.

4.2 Origin of colloidal stability

For MND hydrogenated at 700°C and 750°C, stable suspensions in water were obtained. These suspensions exhibit a positive zeta potential, as for DND treated under hydrogen [16,18]. For H-MND at 750°C and Patm, the stability is excellent over two months. Here, we will detail different possibilities to explain this colloidal stability.

4.2.1 role of sp^2 carbon?

The colloidal stability of H-MND relies on their positive zeta potential, which prevents their sedimentation by repulsive forces. However, the origin of this positive zeta potential on hydrogenated nanodiamonds (synthesized by detonation or by milling) is still subject of debate. In 2017, in one of the very few study of the literature dedicated to the colloidal behavior of hydrogenated MND, Gines et al. stated that the positive zeta potential of their treated particles originates from the protonation of surrounding graphene like shells [22]. In this study, authors demonstrated that a positive zeta potential after hydrogenation (at 500°C and 10 mbar in their case) is only obtained on vacuum-annealed particles (1000°C, 10^{-3} mbar). A straightforward hydrogenation treatment applied on "as received" MND is shown to be inefficient, in their conditions, to get stable particles, as there is not enough sp^2 content on the surface. According to the provided explanations, the vacuum annealing helps to decorate the surface of their particles with sp^2 reconstructions, on which protons will bind and provide a positive charge. In this approach, hydrogenation treatment is only used to desorb oxygenated species initially present (responsible for the negative Zeta potential) and to prevent the spontaneous formation of oxides at the MND surface by saturating the dangling bonds. Indeed, HR-TEM pictures of their graphitized + hydrogenated MND exhibit clear graphitic reconstruction and amorphous carbon on their surface, confirmed by Raman spectroscopy (recorded at 532 nm) with quite intense G and D bands compared to the first order diamond peak and the signature of trans-polyacetylene structures.

In our system, straightforward hydrogenation was efficient to provide colloidal stability to MND when 700°C at least is reached during the H_2 annealing, whatever the pressure of H_2 (even at 10 mbar as for Gines et al.). Concerning the origin of our positive Zeta Potential, the role of protonated graphene like reconstruction has to be debated. On our H-MND, HR-TEM evidence very clean faceted particles, with diamond planes reaching the extreme surface of the crystallites. Obviously, microscopy remains a local characterization technique, however tens of particles were studied in this work and none of them exhibited any graphitic reconstruction or amorphous carbon on their periphery when hydrogenated. Rather, at least in our conditions, hydrogen annealing even tends to show etching of non-diamond phases from the surface of the particles, as confirmed by XPS. From 4% of the overall carbon signal on our initial oxidized particles, the proportion of C=C can be reduced down to 1% in the harsher conditions, while keeping perfect colloidal stability. This etching behavior is even more pronounced when "as received" MND were directly hydrogenated at 750°C and atmospheric pressure, with a drastic reduction of the C=C component from 9% down to 1% (SI Figure S3). Here as well, the non-diamond carbon

related peak at 11 eV in the BV support this observation. Looking at our Raman spectra, even if H-MND exhibit a little more pronounced G band than Ox-MND (already discussed above), we keep an intense and narrow first order diamond peak. Taking into account all these observations, it is clear that our H-MND exhibit very low amount of sp^2 reconstructions, and definitely much less than the ones of Gines et al. as clearly evidenced when comparing Raman spectra. Thus, using our hydrogenation conditions, the positive zeta potential finally obtained is rather unlikely to originate from protonated graphene-like reconstructions.

4.2.2 Role of different facets?

To further understand the origin of the colloidal stability of our H-MND, the differences in chemical signature of sediments (unstable particles) and supernatants (stable particles) were worth studying. We first compared the presence of oxidized functions on stable and unstable particles. On this point, FTIR exhibits similar trends for both types of particles, with the vanishing of the C=O and C-O stretching modes when temperature of annealing is raised. To be more quantitative, XPS analysis was performed on the supernatant and the sediment of sonicated and centrifuged hydrogen-treated particles at 750°C. Very low amount of oxygen was measured on both stable and unstable H-MND (1.1 at % vs. 2 at % respectively) and deconvolution of the C1s core levels were very similar. Therefore, a lower electrostatic potential due to the remaining of oxidized functions to explain the instability of a part of our treated particles can be reasonably excluded.

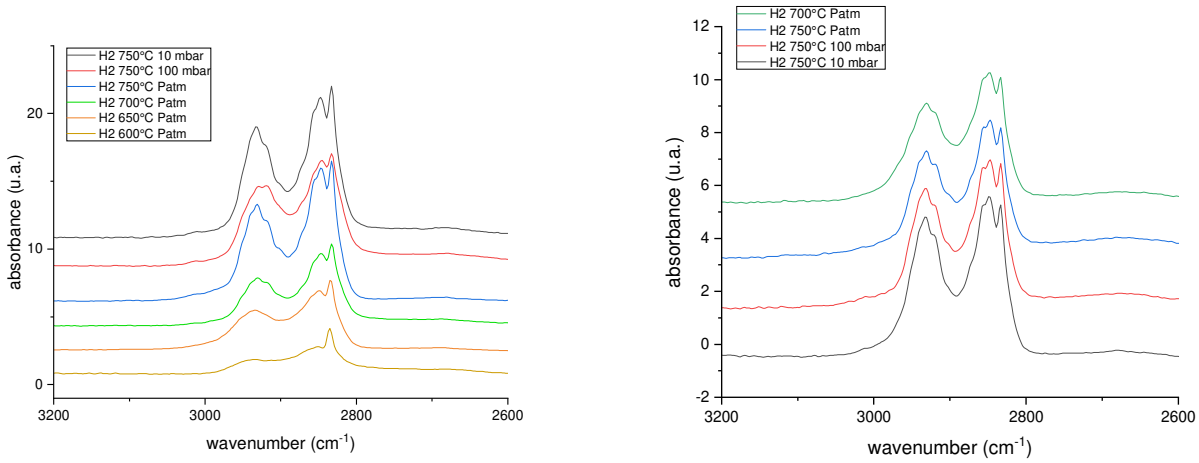

Figure 11 : FTIR C-H stretching modes of (left) sediments and (right) supernatants of hydrogenated MND at 700°C and 750°C at Patm, 100 mbar and 10mbar

If we now focus on the shape of the C-H stretching modes of the FTIR spectra of stable and unstable particles, a clear difference is visible (Figure 11). As already detailed above, the ratio between the 2850

and 2930 cm^{-1} peaks and the one at 2830 cm^{-1} is modified. Sediments always exhibit more intense 2830 cm^{-1} peak, which signs for the C-H terminations on (111) facet. In their papers published in the early 2000s [38, 39, 40], H.-C. Chang and C.-L. Cheng evidenced a size dependence of the C-H features on diamond nanocrystals. They showed that this 2830 cm^{-1} peak is not visible on 5 nm detonation nanodiamonds and only becomes visible when raising the size of the diamond nanocrystallite up to tens of nm. They explained this phenomenon by the very low amount of (111) facets on particles smaller than 5 nm. Then, comparing particles from 35 nm to 350 nm, they evidenced a strong increase of the 2830 cm^{-1} peak intensity in the C-H stretching modes. In our study, we used polydispersed MND with crystallites sizes ranging from few nm up to 50 nm (SI, Figure S5). In order to check if the smaller C-H peak related to hydrogenated (111) facet of the supernatants stands for an elimination of the larger particles, XRD analyses were performed. We compared particles out of the furnace after hydrogen annealing (before sonication) and particles remaining in the sediment (diffractograms available in SI Figure S6). Due to the amount of material necessary to perform XRD, analysis of the particles in the supernatant was not allowed. From (111) diffraction peak, applying the Scherrer equation, we estimated the mean crystalline domain size of the particles, given in Table 3. Considering the uncertainty of applying Scherrer formula on nanocrystals [44], we noticed that sediment contained particles with a mean diameter in the same order of magnitude than the one of particles out of the furnace. This observation does not argue for an important size sorting of the H-MND during the centrifugation, leaving the bigger crystallites in the sediment.

	Ox-MND	**H-MND 750°C Patm**	**H-MND 750°C 100 mbar**
Mean size of H-MND out of the furnace (before sonication)	**12,8 nm**	**13,1 nm**	**13,2 nm**
Mean size of H-MND remaining in the sediment after centrifugation	**11,2 nm**	**11,9 nm**	**12,0 nm**

Table 3: Comparison of mean sizes extracted from (111) diamond diffraction peak for Ox- MND, H-MND at 750°C under atmospheric pressure and 100 mbar

It remains that this exaltation of the C-H peak corresponding to the hydrogen terminations on (111) facets in the supernatant has always been observed as soon as we prepared colloidal suspension of H-MND, for this study and for others. If a size effect is excluded, we may consider a detrimental influence of this facet on the colloidal stability of H-MND. In 2014, theoretical calculations of A. Barnard in collaboration with E. Osawa [45] evidenced the role of each diamond facet on the overall surface charge of nanodiamonds. In their study, they reported on the native negative charge of the (111) facet which may interfere with the overall positive electrostatic potential of their simulated nanodiamond structures. If the calculations were designed for small and quasi-spherical particles, we may envisaged that such negative charge persists on (111) facets on our milled particles, at least for the smallest. The higher proportion of 2830 cm^{-1} peak in the sediment would therefore reflect a destabilization of the electrostatic repulsion between the particles due to a larger proportion of (111) facet. Aggregation of positively charged particles through these (111) facets can also be reasonably considered.

4.3 Signature of a surface conductivity

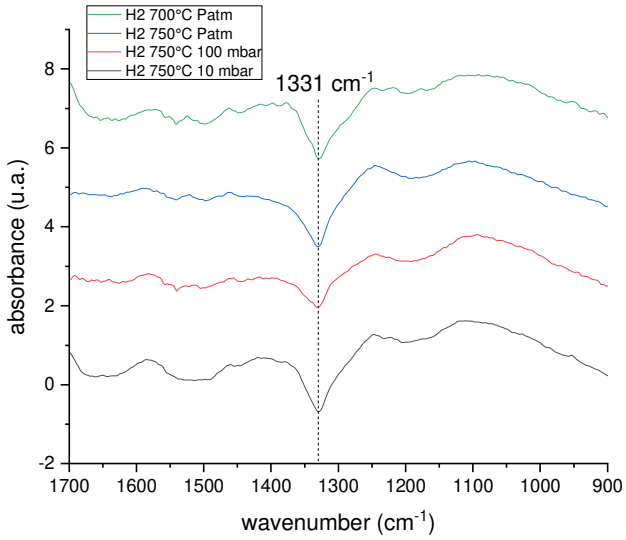

Figure 12: FTIR spectra of supernatants of hydrogenated MND at 750°C at Patm, 100 mbar and 10mbar

Another difference observed on FTIR spectra between stable and unstable particles concerns the presence of a dip in the absorption (transmission window) located at 1331 cm^{-1} only in the supernatants (Figure 12). This phenomenon has been reported very recently in the literature by Kudryavtsev et al. [46] and Ekimov et al. [47] for high quality hydrogenated nanodiamonds. In both studies, authors attributed this transmission window located in the Raman diamond mode to Fano-type destructive interferences between

discrete states of optical phonons and a continuum of electron or hole states appearing at the surface of the hydrogenated nanodiamond. Such effect was already observed on doped single-walled carbon nanotubes [48] or metallic nanoshell particles [49]. However, authors do not agree on the origin of the surface conductivity on ND allowing these Fano interferences. For Kudryavtsev et al., the conductivity comes from the well-known transfer doping arising at hydrogenated diamond surface in contact with ambient atmosphere or water [50, 51]. In this model, a superficial conductive layer is generated by an electrochemical equilibrium between the hydrogenated diamond surface and oxygen-related adsorbates, which promotes an intense band bending and the accumulation of holes at the surface of the material [52]. By this mean, a p-type conductive layer is created at the surface of hydrogenated diamond, even on undoped materials. The alternative origin of the surface conductivity required to induce Fano interferences proposed by Ekimov et al. relies on the reconstruction of the dangling bonds at the surface of their nanodiamonds into a monoatomic layer of graphite. However, as noticed by the authors, these sp^2 reconstructions can only partly explain the surface conductivity of their particles considering the abundance of C-H stretching modes measured at the same time on the same particles.

In our study, the formation of p-type conductive layer at the surface of our nanodiamonds is more likely to occur. Our MND seems to behave like bulk diamond with a shift of their valence and conductive band when hydrogenated, which argue for a similar behavior toward electrochemically active adsorbates and possible band bending. As already explained above, XPS, Raman and HR-TEM performed on H-MND evidence only a very limited amount of graphitic carbon, which does not support the hypothesis of conductivity coming from fully reconstructed nanodiamonds.

Whatever the origin of the conductivity allowing the Fano interferences, it remains that we observed this optical effect only for H-MND stable in suspension. This would mean that unstable and stable H-MND could differ by their surface conductivity, which would affect their colloidal stability. In 2013, we already discussed about the possible role of such surface conductivity to explain the colloidal stability of hydrogenated detonation nanodiamonds [16]. Here, thanks to these nanodiamonds of better crystalline quality, we were able to indirectly probe this surface conductivity by an optical pathway.

4.4 Spatial organization of H-MND in water

As shown by cryo-EM observations, a specific spatial arrangement is observed for H-MND with chain like structures extending at long range. Such chains are often built with joint single particles. A previous cryo-EM study of DND dispersed in water [53] reported on similar chain like structures for oxidized or

hydrogenated particles. The electrostatic interactions between opposite charged facets are supposed to be at the origin of chain formation. Indeed, as explained previously, the different crystallographic (111), (100) and (110) facets can behave opposite charges [45]. According to the more facetted shape of MND, it is pertinent to consider that such differently charged facets are involved in this assembly mechanism. Furthermore, our FTIR results suggest a surface conductivity for H-MND. Its possible role in the chain formation at long range needs to be further investigated.

5. Conclusion

Nanodiamonds synthesized by High Pressure High Temperature diamond milling (MND) were successfully hydrogenated and stabilized in water suspension over two months, with a concentration range of 3-5 mg/mL. The optimal hydrogenation conditions correspond to an annealing at 750°C under atmospheric pressure leading to a minimization of carbon/oxygen bonds and sp^2/amorphous carbon at MND surface as shown by FTIR and XPS. Clean highly crystalline particles were observed by HR-TEM. Stable aqueous suspensions of H-MND were monitored up to two months, exhibiting stable mean hydrodynamic diameter around 30 nm without noticeable sedimentation. The colloidal stability cannot be solely explained by the remaining sp^2 carbon content that is very low (1% of the total C1s area in XPS) but we observed that particles in supernatants exhibited different C-H stretching structures compared to unstable ones according to FTIR. A particular chain-like arrangement was observed by Cryo-EM for H-MND with the formation of chain like structures extending over micron range. The opposite charge of the different crystallographic facets is proposed to be at the origin of the assembly mechanism. Such stable aqueous colloids paves the way to use highly crystalline H-MND that possess assets close to bulk diamond for quantum and photo(electro)catalysis applications.

Acknowledgements

Authors would like to acknowledge CEA for the funding of L. Saoudi PhD.

References

[1] J.-C. Arnault, Nanodiamonds, Elsevier, 2017. https://doi.org/10.1016/C2015-0-01721-X.

[2] V.Y. Dolmatov, Detonation-synthesis nanodiamonds: synthesis, structure, properties and applications, Russ. Chem. Rev. 76 (2007) 339–360. https://doi.org/10.1070/RC2007v076n04ABEH003643.

[3] N. Nunn, M. Torelli, G. McGuire, O. Shenderova, Nanodiamond: A high impact nanomaterial, Current Opinion in Solid State and Materials Science 21 (2017) 1–9

[4] S. L. Y. Chang, P. Reineck, A. Krueger, V. N. Mochalin, Ultrasmall Nanodiamonds: Perspectives and Questions, ACS Nano 16 (2021) 8513-8524.

[5] S. Stehlik, M. Mermoux, B. Schummer, O. Vanek, K. Kolarova, P. Stenclova, A. Vlk, M. Ledinsky, R. Pfeifer, O. Romanyuk, I. Gordeev, F. Roussel-Dherbey, Z. Nemeckova, J. Henych, P. Bezdicka, A. Kromka, B. Rezek, Size effects on surface chemistry and Raman spectra of Sub-5 nm oxidized high-pressure high-temperature and detonation nanodiamonds, J. Phys. Chem. C. 125 (2021) 5647–5669. https://doi.org/10.1021/acs.jpcc.0c09190.

[6] A. Ajoy, R. Nazaryan, E. Druga, K. Liu, A. Aguilar, B. Han, M. Gierth, J.T. Oon, B. Safvati, R. Tsang, J.H. Walton, D. Suter, C.A. Meriles, J.A. Reimer, A. Pines, Room temperature "optical nanodiamond hyperpolarizer ": Physics, design, and operation, Rev. Sci. Instrum. 91 (2020). https://doi.org/10.1063/1.5131655.

[7] K. Turcheniuk, V.N. Mochalin, Biomedical applications of nanodiamond (Review), Nanotechnology. 28 (2017) 252001. https://doi.org/10.1088/1361-6528/aa6ae4.

[8] A. Krueger, Current issues and challenges in surface chemistry of nanodiamonds in Nanodiamonds, Elsevier, 2017. https://doi.org/10.1016/C2015-0-01721-X. 183 - 242

[9] A. Bolker, C. Saguy, R. Kalish, Transfer doping of single isolated nanodiamonds, studied by scanning probe microscopy techniques., Nanotechnology. 25 (2014) 385702. https://doi.org/10.1088/0957-4484/25/38/385702.

[10] F. Maier, M. Riedel, B. Mantel, J. Ristein, L. Ley, Origin of Surface Conductivity in Diamond, Phys. Rev. Lett. 85 (2000) 3472–3475. http://link.aps.org/doi/10.1103/PhysRevLett.85.3472.

[11] L. Zhang, R.J. Hamers, Photocatalytic reduction of CO_2 to CO by diamond nanoparticles, Diam. Relat. Mater. 78 (2017) 24–30. https://doi.org/10.1016/j.diamond.2017.07.005.

[12] N. Nunn, O. Shenderova, Toward a golden standard in single digit detonation nanodiamond, Phys. Status Solidi Appl. Mater. Sci. 213 (2016) 2138–2145. https://doi.org/10.1002/pssa.201600224.

[13] T. Tiainen, T.T.T. Myllymäki, T. Hatanpää, H. Tenhu, S. Hietala, Polyelectrolyte stabilized nanodiamond dispersions, Diam. Relat. Mater. 95 (2019) 185–194. https://doi.org/10.1016/j.diamond.2019.04.019.

[14] C. Bradac, I. Das Rastogi, N.M. Cordina, A. Garcia-Bennett, L.J. Brown, Influence of surface composition on the colloidal stability of ultra-small detonation nanodiamonds in biological media, Diam. Relat. Mater. 83 (2018) 38–45. https://doi.org/10.1016/j.diamond.2018.01.022.

[15] T. Wang, S. Handschuh-Wang, S. Zhang, X. Zhou, Y. Tang, Enhanced nucleation of diamond on three dimensional tools via stabilized colloidal nanodiamond in electrostatic self-assembly seeding process, J. Colloid Interface Sci. 506 (2017) 543–552. https://doi.org/10.1016/j.jcis.2017.07.035.

[16] T. Petit, H. A. Girard, A. Trouvé, I. Batonneau-Gener, P. Bergonzo, J.-C. Arnault, Surface transfer doping can mediate both colloidal stability and self-assembly of nanodiamonds., Nanoscale. 5 (2013) 8958–62. https://doi.org/10.1039/c3nr02492j.

[17] F. Ducrozet, H.A. Girard, J. Leroy, E. Larquet, I. Florea, E. Brun, C. Sicard-Roselli, J.-C. Arnault, New Insights into the Reactivity of Detonation Nanodiamonds during the First Stages of Graphitization, Nanomaterials. 11 (2021) 2671. https://doi.org/10.3390/nano11102671.

[18] J.C. Arnault, H.A. Girard, Hydrogenated nanodiamonds: Synthesis and surface properties, Curr. Opin. Solid State Mater. Sci. 21 (2017) 10–16. https://doi.org/10.1016/j.cossms.2016.06.007.

[19] S. Claveau, É. Nehlig, S. Garcia-Argote, S. Feuillastre, G. Pieters, H.A. Girard, J.-C. Arnault, F. Treussart, J.-R. Bertrand, Delivery of siRNA to Ewing Sarcoma Tumor Xenografted on Mice, Using Hydrogenated Detonation Nanodiamonds: Treatment Efficacy and Tissue Distribution, Nanomaterials. 10 (2020) 553. https://doi.org/10.3390/nano10030553.

[20] T. Petit, L. Puskar, T. Dolenko, S. Choudhury, E. Ritter, S. Burikov, K. Laptinskiy, Q. Brzustowski, U. Schade, H. Yuzawa, M. Nagasaka, N. Kosugi, M. Kurzyp, A. Venerosy, H. Girard, J.-C. Arnault, E. Osawa, N. Nunn, O. Shenderova, E.F. Aziz, Unusual Water Hydrogen Bond Network around Hydrogenated Nanodiamonds, J. Phys. Chem. C. 121 (2017) 5185–5194. https://doi.org/10.1021/acs.jpcc.7b00721.

[21] S. Stehlik, T. Glatzel, V. Pichot, R. Pawlak, E. Meyer, D. Spitzer, B. Rezek, Water interaction with hydrogenated and oxidized detonation nanodiamonds — Microscopic and spectroscopic analyses,

Diam. Relat. Mater. 63 (2016) 97–102. https://doi.org/http://dx.doi.org/10.1016/j.diamond.2015.08.016.

[22] L. Ginés, S. Mandal, A.-I.-A. Ashek-I-Ahmed, C.-L. Cheng, M. Sow, O.A. Williams, L. Gines, S. Mandal, A.-I. Ahmed, C.-L. Cheng, M. Sow, O.A. Williams, Positive zeta potential of nanodiamonds, Nanoscale. 9 (2017) 12549–12555. https://doi.org/10.1039/C7NR03200E.

[23] V. V Korolkov, I.I. Kulakova, B.N. Tarasevich, G. V Lisichkin, Dual reaction capacity of hydrogenated nanodiamond, Diam. Relat. Mater. 16 (2007) 2129–2132. https://doi.org/http://dx.doi.org/10.1016/j.diamond.2007.07.018.

[24] O.A. Williams, J. Hees, C. Dieker, W. Jäger, L. Kirste, C.E. Nebel, Size-Dependent Reactivity of Diamond Nanoparticles, ACS Nano. 4 (2010) 4824–4830. https://doi.org/10.1021/nn100748k.

[25] G. Thalassinos, A. Stacey, N. Dontschuk, B.J. Murdoch, E. Mayes, H.A. Girard, I.M. Abdullahi, L. Thomsen, A. Tadich, J. Arnault, V.N. Mochalin, B.C. Gibson, P. Reineck, Fluorescence and Physico-Chemical Properties of Hydrogenated Detonation Nanodiamonds, C — J. Carbon Res. 6 (2020) 7. https://doi.org/10.3390/c6010007.

[26] L. Schmidlin, V. Pichot, M. Comet, S. Josset, P. Rabu, D. Spitzer, Identification, quantification and modification of detonation nanodiamond functional groups, Diam. Relat. Mater. 22 (2012) 113–117

[27] T. Petit, L. Puskar, FTIR spectroscopy of nanodiamonds: Methods and interpretation, Diam. Relat. Mater. 89 (2018) 52–66. https://doi.org/10.1016/j.diamond.2018.08.005.

[28] J.C. Arnault, X-ray Photoemission Spectroscopy applied to nanodiamonds: From surface chemistry to in situ reactivity, Diam. Relat. Mater. 84 (2018) 157–168. https://doi.org/10.1016/j.diamond.2018.03.015.

[29] E. Vanhove, J. de Sanoit, J.C. Arnault, S. Saada, C. Mer, P. Mailley, P. Bergonzo, M. Nesladek, Stability of H-terminated BDD electrodes: an insight into the influence of the surface preparation, Phys. Status Solidi. 204 (2007) 2931–2939. http://dx.doi.org/10.1002/pssa.200776340.

[30] H. Girard, N. Simon, D. Ballutaud, M. Herlem, A. Etcheberry, Effect of anodic and cathodic treatments on the charge transfer of boron doped diamond electrodes, Diam. Relat. Mater. 16 (2007) 316–325. https://doi.org/10.1016/j.diamond.2006.06.009.

[31] D.S. Knight, W.B. White, Characterization of diamond films by Raman spectroscopy, J. Mater. Res. 4 (1989) 385–393. https://doi.org/10.1557/JMR.1989.0385.

[32] S. Prawer, R. J. Nemanich, Raman spectroscopy of diamond and doped diamond, Phil. Trans. R. Soc. Lond. A (2004) 362, 2537–2565

[33] R. Arenal, G. Montagnac, P. Bruno, D.M. Gruen, Multiwavelength Raman spectroscopy of diamond nanowires present in n -type ultrananocrystalline films, Phys. Rev. B - Condens. Matter Mater. Phys. 76 (2007) 3–8. https://doi.org/10.1103/PhysRevB.76.245316.

[34] Mermoux, M.; Crisci, A.; Petit, T.; Girard, H.A.; Arnault, J.-C. Surface Modifications of Detonation Nanodiamonds Probed by Multiwavelength Raman Spectroscopy. J. Phys. Chem. C 2014, 118, 23415–23425.

[35] J. Stetefeld, S. A. McKenna, T. R. Patel, Dynamic light scattering: a practical guide and applications in biomedical sciences, Biophys Rev (2016) 8:409–427

[36] D. Lin-Vien, N.B. Colthup, W.G. Fateley, J.G. Grasselli, The Handbook of Infrared and Raman Characteristic Frequencies of Organic Molecules (1991).

[37] T. Jiang, K. Xu, S. Ji, S. Jib, FTIR studies on the spectral changes of the surface functional groups of ultradispersed diamond powder synthesized by explosive detonation after treatment in hydrogen, nitrogen, methane and air at different temperatures, J. Chem. Soc. Faraday Trans. 92 (1996) 3401–3406. https://doi.org/10.1039/FT9969203401.

[38] Y.-R. Chen, H.-C. Chang, C.-L. Cheng, C.-C. Wang, J.C. Jiang, Size dependence of CH stretching features on diamond nanocrystal surfaces: Infrared spectroscopy and density functional theory calculations, J. Chem. Phys. 119 (2003) 10626–10632. http://dx.doi.org/10.1063/1.1620503.

[39] A.P. Jones, L.B. d'Hendecourt, S.-Y. Sheu, H.-C. Chang, C.-L. Cheng, H.G.M. Hill, Surface C-H stretching features on meteoritic nanodiamonds, A&A. 416 (2004) 235–241. http://dx.doi.org/10.1051/0004-6361:20031708.

[40] C.-L. Cheng, C.-F. Chen, W.-C. Shaio, D.-S. Tsai, K.-H. Chen, The CH stretching features on diamonds of different origins, Diam. Relat. Mater. 14 (2005) 1455–1462. https://doi.org/10.1016/j.diamond.2005.03.003.

[41] G. Speranza, S. Torrengo, L. Minati, M. Filippi, M. Castellino, C. Manfredotti, C. Manfredotti, M. Dipalo, A. Pasquarelli, E. Kohn, H. El-Hajj, E. Vittone, Characterization of UV irradiated nanocrystalline diamond, Diam. Relat. Mater. 17 (2008) 1194–1198. https://doi.org/10.1016/j.diamond.2008.01.098.

[42] J.I.B. Wilson, J.S. Walton, G. Beamson, Analysis of chemical vapour deposited diamond films by

X-ray photoelectron spectroscopy, J. Electron Spectros. Relat. Phenomena. 121 (2001) 183–201. https://doi.org/10.1016/S0368-2048(01)00334-6.

[43] S. Kaciulis, A. Mezzi, P. Calvani, D.M. Trucchi, Electron spectroscopy of the main allotropes of carbon, Surf. Interface Anal. 46 (2014) 966–969. https://doi.org/10.1002/sia.5382.

[44] A. Monshi, M.R. Foroughi, M.R. Monshi, Modified Scherrer Equation to Estimate More Accurately Nano-Crystallite Size Using XRD, World J. Nano Sci. Eng. 02 (2012) 154–160. https://doi.org/10.4236/wjnse.2012.23020.

[45] A.S. Barnard, E. Ōsawa, The impact of structural polydispersivity on the surface electrostatic potential of nanodiamond, Nanoscale. 6 (2014) 1188–1194. https://doi.org/10.1039/C3NR05344J.

[46] O.S. Kudryavtsev, R.H. Bagramov, A.M. Satanin, A.A. Shiryaev, O.I. Lebedev, A.M. Romshin, D.G. Pasternak, A. V. Nikolaev, V.P. Filonenko, I.I. Vlasov, Fano-type Effect in Hydrogen-Terminated Pure Nanodiamond, Nano Lett. 22 (2022) 2589–2594. https://doi.org/10.1021/acs.nanolett.1c04887.

[47] E. Ekimov, A.A. Shiryaev, Y. Grigoriev, A. Averin, E. Shagieva, S. Stehlik, M. Kondrin, Size-Dependent Thermal Stability and Optical Properties of Ultra-Small Nanodiamonds Synthesized under High Pressure, Nanomaterials. 12 (2022) 1–22. https://doi.org/10.3390/nano12030351.

[48] F. Lapointe, I. Gaufrès, I. Tremblay, N.Y.W. Tang, R. Martel, P. Desjardins, Fano resonances in the midinfrared spectra of single-walled carbon nanotubes, Phys. Rev. Lett. 109 (2012) 1–5. https://doi.org/10.1103/PhysRevLett.109.097402.

[49] P. Gu, X. Cai, G. Wu, C. Xue, J. Chen, Z. Zhang, Z. Yan, F. Liu, C. Tang, W. Du, Z. Huang, Z. Chen, Ultranarrow and tunable fano resonance in ag nanoshells and a simple ag nanomatryushka, Nanomaterials. 11 (2021). https://doi.org/10.3390/nano11082039.

[50] M.I. Landstrass, K. V Ravi, Resistivity of chemical vapor deposited diamond films, Appl. Phys. Lett. 55 (1989) 975–977. http://dx.doi.org/10.1063/1.101694.

[51] R.S. Gi, T. Mizumasa, Y. Akiba, Y. Hirose, T. Kurosu, M. Ilda, Formation mechanism of p-type surface conductive layer on deposited diamond films, Jpn. J. Appl. Phys. 34 (1995) 5550–5555. https://doi.org/10.1143/JJAP.34.5550.

[52] P. Strobel, M. Riedel, J. Ristein, L. Ley, Surface transfer doping of diamond., Nature. 430 (2004) 439–41. https://doi.org/10.1038/nature02751.

[53] S.L.Y. Chang, P. Reineck, D. Williams, G. Bryant, G. Opletal, S.A. El-Demrdash, P.L. Chiu, E. Osawa, A.S. Barnard, C. Dwyer, Dynamic self-assembly of detonation nanodiamond in water, Nanoscale. 12 (2020) 5363–5367. https://doi.org/10.1039/c9nr08984e.

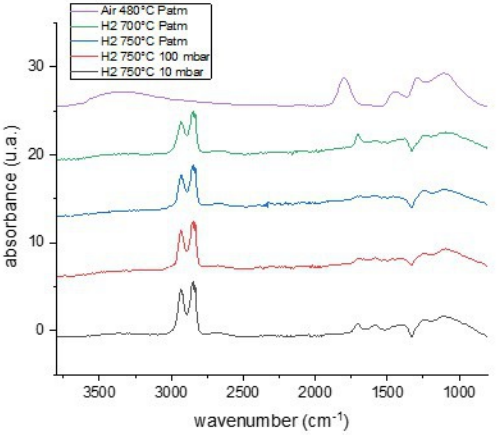
Air 480°C Patm
H2 700°C Patm
H2 750°C Patm
H2 750°C 100 mbar
H2 750°C 10 mbar
absorbance (u.a.)
wavenumber (cm-1)

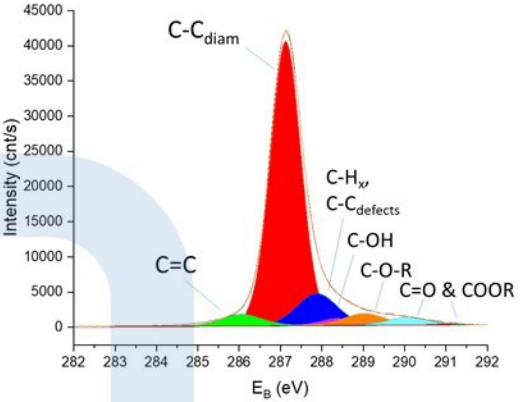
C-Cdiam
C-Hx,
C-Cdefects
C-OH
C-O-R
C=O & COOR
C=C
Intensity (cnt/s)
EB (eV)

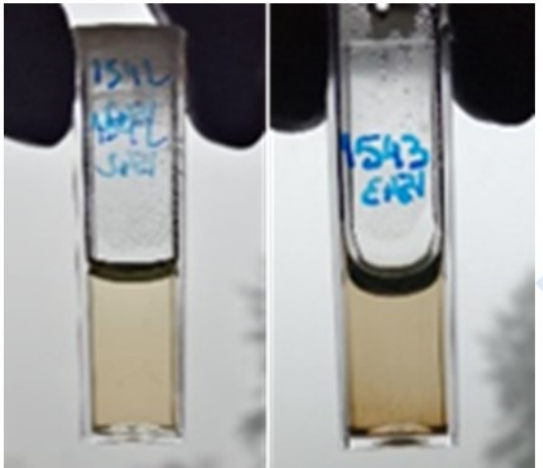

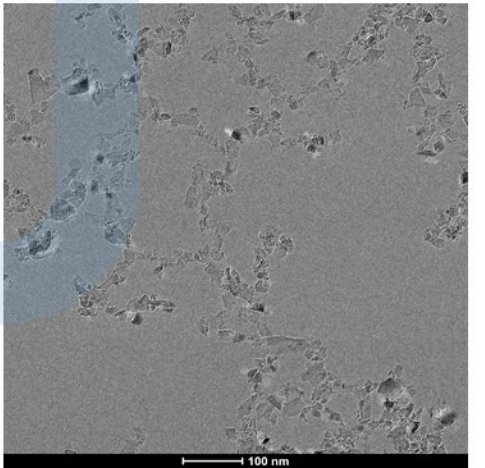
100 nm